VII. Preliminary results for global linear stability theory (LST)

ADflow has not been previously used for LST. Therefore, we have used the canonical cylinder flow vortex shedding case to benchmark our results against literature. In this section, we present the LST for ADflow and results for the unsteady cylinder vortex shedding and steady base flow LST derived eigenfrequencies.

The governing equations for Navier–Stokes solved in ADflow can be summarized as

$$\mathbf{r}_k(\mathbf{w}) = 0, \tag{44}$$

where $\mathbf{w}$ is the state vector and $\mathbf{r}_k$ is the residual. For steady state base flow solution $\bar{\mathbf{w}}$, we have for a small increment in time

$$\frac{\mathrm{d}\mathbf{w}}{\mathrm{d}t} = -\mathbf{M}^{-1}\mathbf{r}_k(\mathbf{w}), \tag{45}$$

where $\mathbf{M}$ is the mass matrix from the FVM solver. All terms on RHS are treated implicitly for the Newton's method. In ADflow, the mass matrix is invoked into the residual by dividing by cell volumes. Therefore, the equation becomes

$$\frac{\mathrm{d}\mathbf{w}}{\mathrm{d}t} = -\mathbf{r}(\mathbf{w}), \tag{46}$$

where $\mathbf{r} = \mathbf{M}^{-1}\mathbf{r}_k$. Now, this can be expanded as

$$\begin{aligned} &\frac{\mathrm{d}(\bar{\mathbf{w}} + \delta\mathbf{w})}{\mathrm{d}t} = -\mathbf{r}(\bar{\mathbf{w}} + \delta\mathbf{w}), \\ \implies &\frac{\mathrm{d}\delta\mathbf{w}}{\mathrm{d}t} = -\left(\mathbf{r}(\bar{\mathbf{w}}) + \frac{\partial \mathbf{r}}{\partial \mathbf{w}}_{|\bar{\mathbf{w}}}\right), \\ \implies &\frac{\mathrm{d}\delta\mathbf{w}}{\mathrm{d}t} = -\mathbf{J}\delta\mathbf{w}, \end{aligned} \tag{47}$$

where we linearized and neglected the higher order terms. Assuming a modal ansatz $\delta\mathbf{w} = \mathbf{\Phi}\mathrm{e}^{\lambda t}$, and substituting that in the above equation, we get

$$-\mathbf{J}\mathbf{\Phi} = \lambda\mathbf{\Phi}. \tag{48}$$

This is the final equation which is an eigenvalue problem. Solving this equation gives us the eigenvalues. The eigenvalue can be written in the following manner

$$\lambda = \lambda_r + i\lambda_i, \tag{49}$$

where λ_r and λ_i are the real and complex–valued parts of the eigenvalue. For unstable flow exhibiting the Hopf bifurcation and entering into saturated limit–cycle oscillations, we typically see a complex conjugate pair of eigenvalues with a positive real part [10, 31].

It is a fact that ADflow non–dimensionalizes the governing equations. The eigenvalues sought are therefore non–dimensional. To re–dimensionalize the eigenvalues to help compare with literature, we must scale them by the factor

$$\lambda_s = \frac{\lambda}{t_{\mathrm{ref}}}, \tag{50}$$

where λ_s is the scaled eigenvalue and

$$t_{\mathrm{ref}} = \mathrm{L}_{\mathrm{ref}}\frac{1}{\sqrt{\mathrm{RT}}}, \tag{51}$$

where R is the gas constant 287 J/kgK, T is the reference temperature 300 K and $\mathrm{L}_{\mathrm{ref}}$ is set to a value of 1 m. λ_s is in rad/s. To convert it into physical frequency, we divide it by 2π.

A structured grid was generated for a cylinder of diameter 1 m. The grid is shown below in the first sub–figure (left) in Figure 6. The domain was discretized with 385 elements in both the circumferential and radial directions. A boundary layer grid near to the cylinder wall was made, as shown in the second sub–figure (right) in Figure 6. The off-wall spacing of the first cell normal to the cylinder is $\Delta r = 10^{-5}$m. The grid is similar to that used in literature [32, 33].

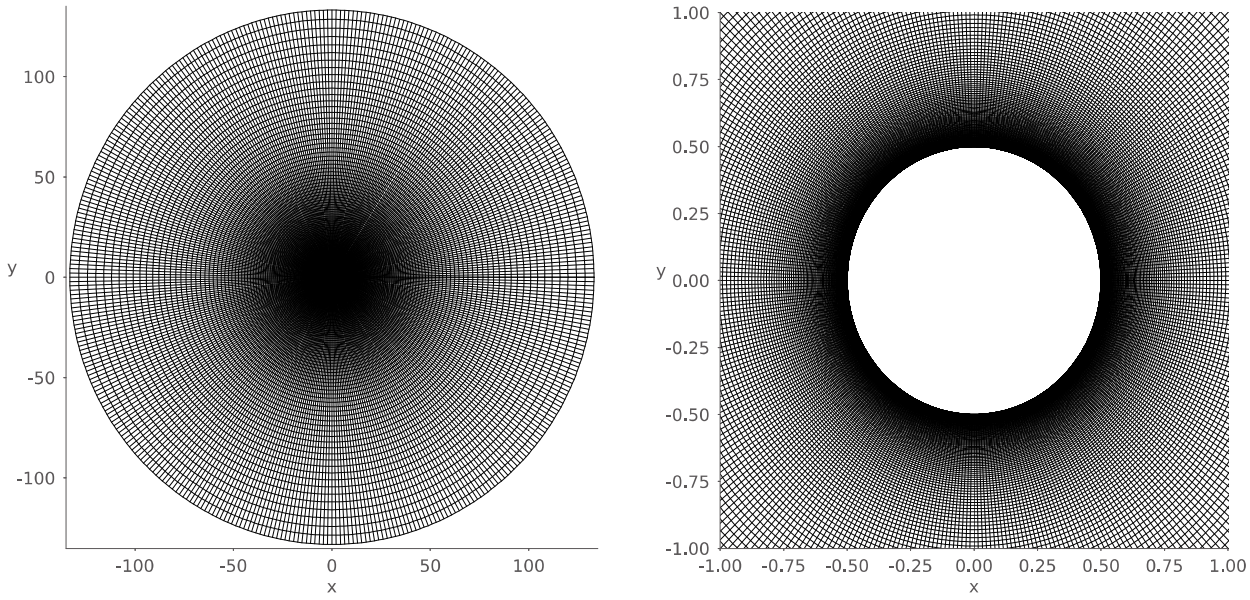

Fig. 6 The full structured grid for the cylinder flow (left) and the grid near the cylinder wall region zoomed in (right). A boundary layer grid is made with the first cell normal to the cylinder wall $\Delta r = 10^{-5}$m. The cylinder diamter is set to 1 m.

Unsteady simulations were run with the laminar Navier Stokes model. The freestream conditions are Mach number of 0.1, Reynolds number in the range 46–120 and temperature of 300 K. A snapshot of the vortex shedding is shown in Figure 7, for a Reynolds number of 100. A classic Von–Karman vortex street is seen behind the cylinder and the flow is in a saturated limit cycle, as seen in the lift–coefficient C_L vs time plot in Figure 7. A small perturbation was made around the base flow, by rotating the cylinder five degrees in one second of physical time. This pushes the system into the saturated limit cycle oscillations.

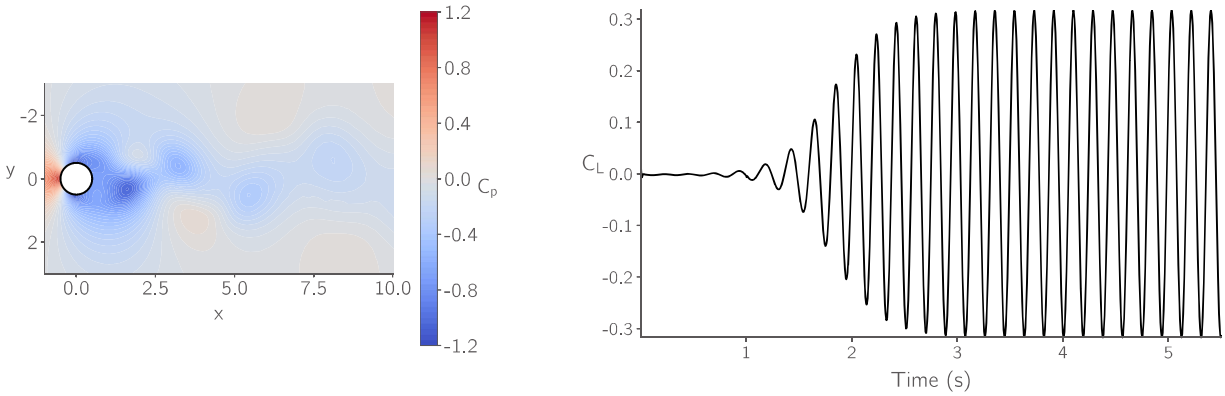

Fig. 7 Unsteady vortex shedding at Reynolds number 100 (left). The Von–Karman vortex street is seen formed inside the saturated limit cycle. The unsteady lift coefficient vs time plot is presented(right). Initial perturbations from the cylinder rotation about base flow grow and saturate into the limit cycle oscillations. The unsteady shedding frequency derived Strouhal number is computed to be 0.163 for Reynolds number 100.

The Strouhal number is defined as

$$\mathrm{St} = \frac{f}{\mathrm{LU}}, \tag{52}$$

where $\mathrm{L} = \mathrm{L}_{\mathrm{ref}} = 1\mathrm{m}$, $\mathrm{U} = 34.718\ \mathrm{m/s}$ and f is the vortex shedding frequency in Hz. In our simulations, we measure this frequency as the frequency of one complete oscillation of the lift–coefficient when the flow has entered into a fully saturated limit cycle.

A plot of the Strouhal number vs Reynolds number is shown in Figure 8 below. We compare our results with Williamson's results [34]. Our results match appreciably with the Hopf–bifurcation diagram from literature.

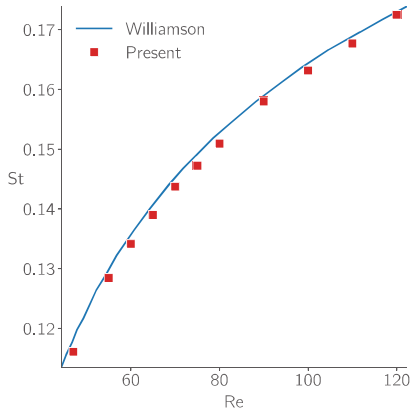

Fig. 8 A plot of the Strouhal numbers evaluated at different Reynolds numbers for the cylinder vortex shedding case. A comparison is made against Williamson's results [34] and the data agrees appreciably.

Finally, we present a plot of the eigenfrequencies from our LST with ADflow in Figure 9. We compare our results with Marquet et al [10]. Our results match to almost machine precision with their results. It should also be noted that the first unstable eigenpair was observed at the critical Reynolds number 46.85, which is very close to Marquet et al [10] who reported the critical Reynolds number to be 46.8±0.05. We also present the modes $\hat{u}$ and $\hat{v}$, the x and y velocity modes in Figure 10. Complex eigenmodes can be scaled and rotated in the complex plane for the same eigenvalues [35] and therefore are not expected to always match with the results from other solvers. The difference in the modes is typically a result of normalization factor used, or whether the mode was at all normalized to begin with. Nevertheless, the mode shapes match appreciably.

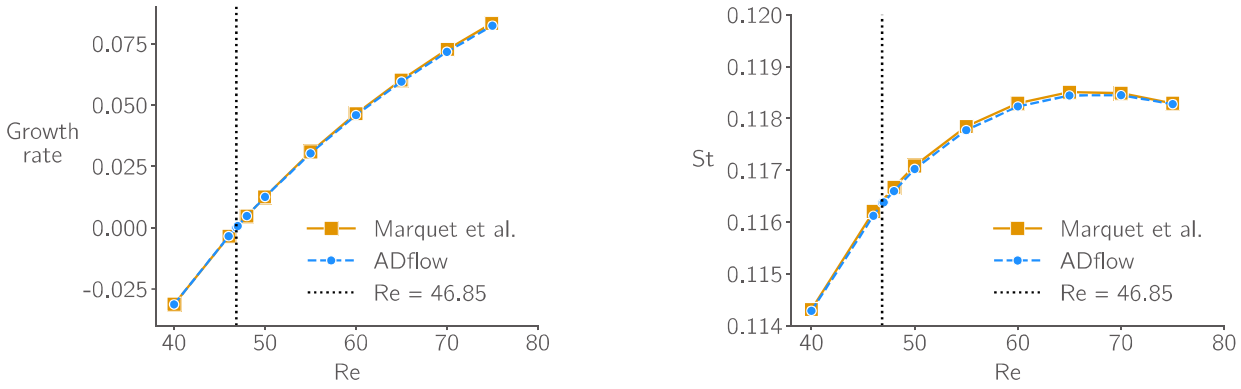

Fig. 9 The growth rates (left) and the eigenfrequency derived Strouhal numbers (right) for the base flow computed at different Reynolds numbers. Results from ADflow are benchmarked against those of Marquet et al. [10], which seem to match appreciably. The critical Reynolds number is found to be 46.85.

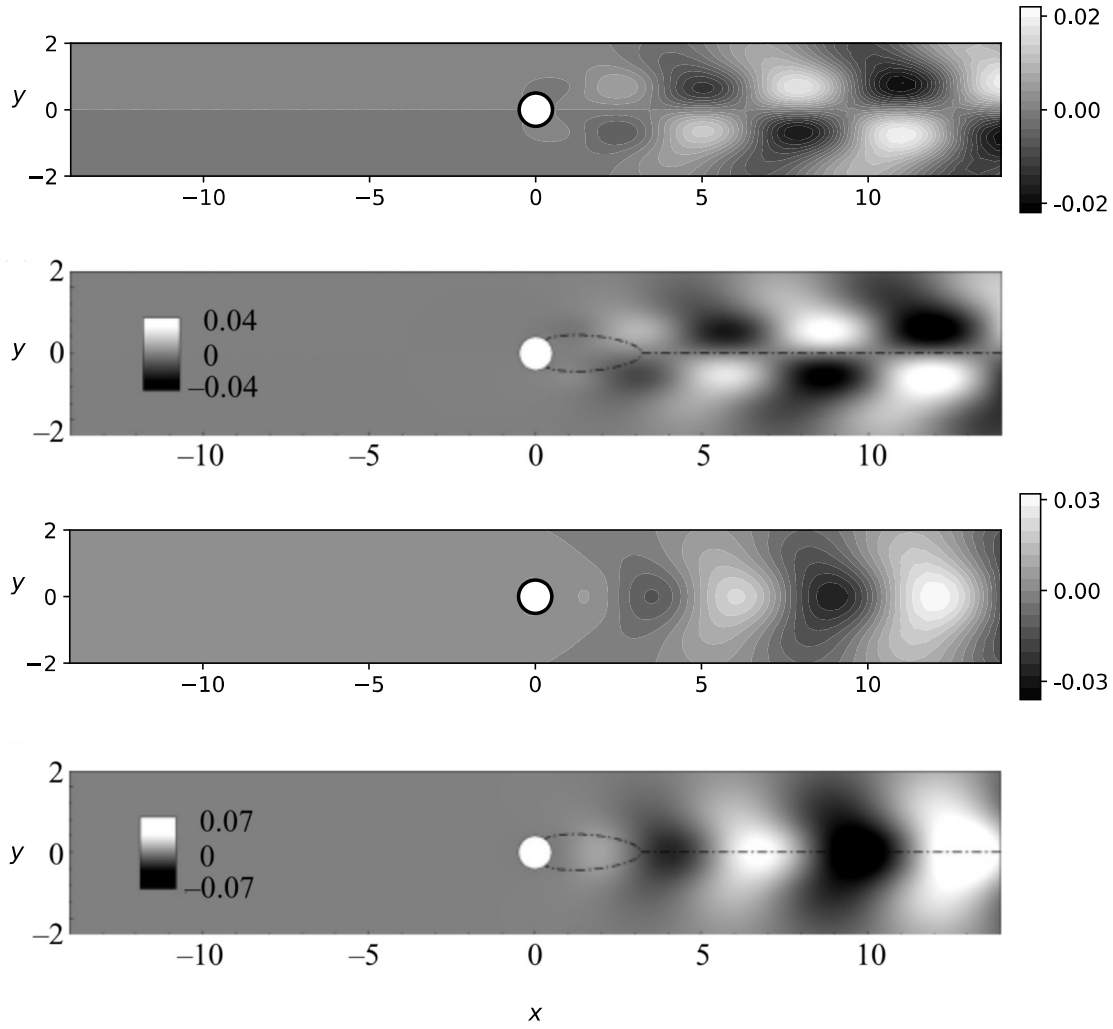

Fig. 10 Unstable eigenmodes from ADflow (from top) are shown in the first and third figures for $\hat{u}$ and $\hat{v}$ respectively, at the critical Reynolds number 46.85 evaluated in the current study. The results from Marquet et al. [10] are shown in the second and fourth figures for $\hat{u}$ and $\hat{v}$ respectively, at the critical Reynolds number 46.8 evaluated in their study.

All simulations and results were converged to tolerance ($< 10^{-12}$), including the eigensolver used–SLEPc, using the shift–invert strategy. The complex part of eigenfrequencies (presented as Strouhal number) do not match with the unsteady Strouhal numbers as shown in Figures 8 and 9. This is a classic case of mean flow and base flow being different, leading to different unstable unsteady frequencies and base flow eigenfrequencies [36, 37].

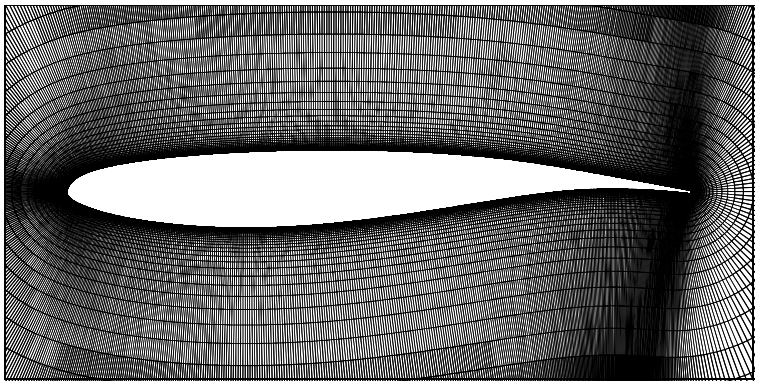

Fig. 11 The full structured grid for the OAT15A transonic airfoil zoomed in on the airfoil wall. A boundary layer grid is made with the first cell normal to the cylinder wall $\Delta r = 10^{-6}$m. The airfoil chord is set to 1 m.

Next, we present the simulation for the transonic buffet 2–D case of OAT15A airfoil [38] and present the grid in Figure 11. The airfoil chord is 1m and We simulated it for Reynolds number 3.2×10^6, Mach number of 0.73 and angle of attack 4°. The unsteady results are shown in Figures 12 and 13, where we present the full unsteady buffet cycle and density contours over one–limit cycle and the unsteady lift coefficent vs time plot.

It is observed that with a cold–start for the simulation, the system readily jumps into a limit–cycle oscillation. The Strouhal number for this setup is computed to be 0.074, which is close to the value reported by Sartor et al [39]. LST was performed on the transonic buffet case by simulating at same conditions for steady base flow. The base flow and the unstable eigenmode are presented in Figure 14. The unstable non–dimensional eigenvalues for this base flow are 0.1±0.445j. The Strouhal number from this eigenfrequency is computed to be 0.045, which slightly under predicts the eigenfrequency computed by Sartor et al [39].

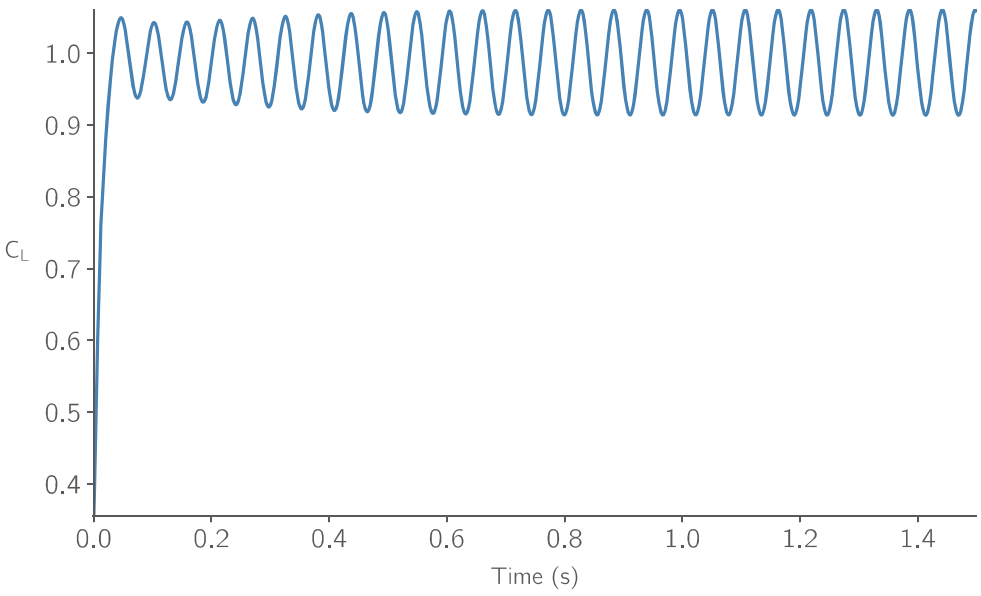

Fig. 12 The unsteady transonic buffetting oscillations presented for OAT15A airfoil at Mach number 0.73, Reynolds number 3.2×10^6 angle of attack 4.0°. The system readily enters into the limit cycle from cold–started simulation. The Strouhal number is computed to be 0.074.

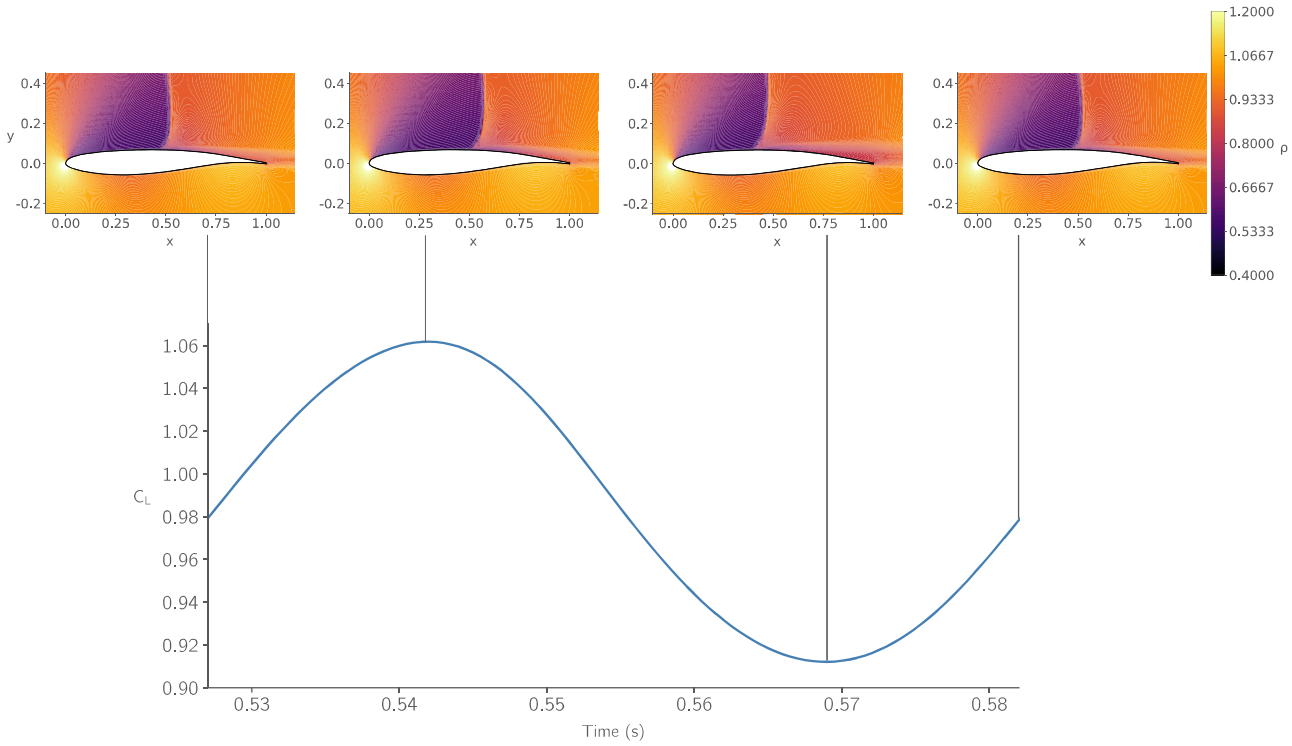

Fig. 13 The unsteady simulation density contours over one cycle in the saturated limit cycle oscillations for the OAT15A transonic airfoil. Freestream conditions are Mach number 0.73, Reynolds number 3.2×10^6 angle of attack 4.0°. Four plots have been made, each at distinct physical times on the limit cycle, indicated by vertical solid black lines from the sinusoidal wave. The Strouhal number for this unsteady transonic buffet is 0.074.

It is a fact that the OAT15A transonic buffet phenomomen is weakly non–linear [39–41]. This means that the mean and base flows are almost identical, leading to the same Strouhal numbers computed from the unsteady limit cycle frequency and the base flow's LST derived eigenfrequency. Our current focus is to investigate this with ADflow and benchmark the LST results for transonic buffet. The unstable eigenmode for this pair of eigenvalues is shown in Figure 14. The shock region right in front of the shock, aft shock, shock foot and the separation bubble appear in the unstable eigenmode. Of all the regions mentioned, the shock by itself dominates over the other flow structures of the eigenmode in magnitude. These flow structures form part of the leading instabilty mechanism for transonic buffet.

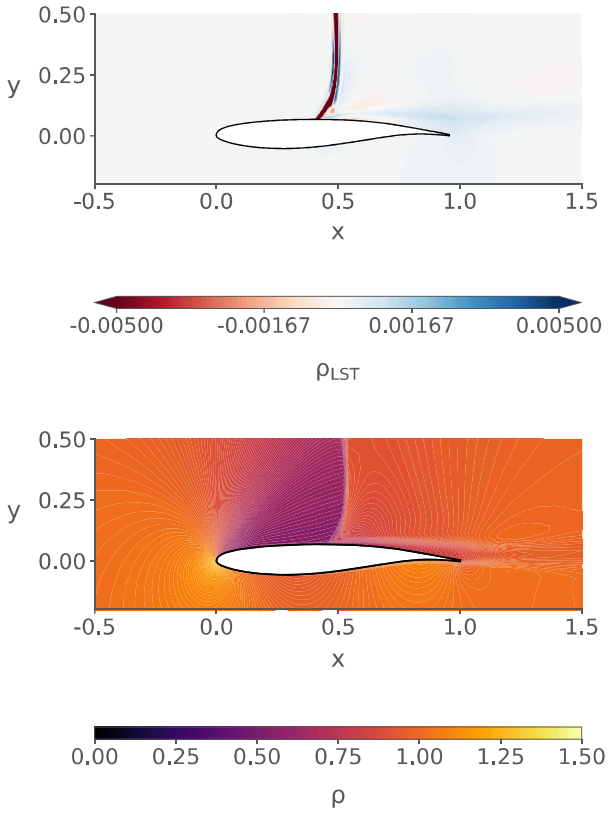

Fig. 14 The density contour for base flow of OAT15A transonic airfoil for Mach number 0.73, Reynolds number 3.2×10^6 angle of attack 4.0° (bottom) and its corresponding unstable eigenmode (top). The regions of the shock, shock foot and separation bubble appear in the unstable eigenmode, indicating the leading flow structures in the instability phenomomen.

References

[1] Church, K. E. M., and Liu, X., "Cost-Effective Robust Stabilization and Bifurcation Suppression," *SIAM Journal on Control and Optimization*, Vol. 57, No. 3, 2019, pp. 2240–2268. doi:10.1137/18M1213142.

[2] Plante, F., Dandois, J., and Laurendeau, É., "ZDES and URANS Simulations of 3D Transonic Buffet Over Infinite Swept Wings," *Progress in Hybrid RANS-LES Modelling*, Springer International Publishing, 2019, pp. 259–269. doi:10.1007/978-3-030-27607-2_21.

[3] Thomas, J., and Dowell, E. H., "Methodology for Numerically Stabilizing a Harmonic Balance Based Aeroelastic Solution Approach," *AIAA Scitech 2020 Forum*, American Institute of Aeronautics and Astronautics, 2020.

[4] Thomas, J. P., Dowell, E. H., and Hall, K. C., "Nonlinear Inviscid Aerodynamic Effects on Transonic Divergence, Flutter, and Limit-Cycle Oscillations," *AIAA Journal*, Vol. 40, No. 4, 2002, pp. 638–646. doi:10.2514/2.1720, URL http://dx.doi.org/10.2514/2.1720.

[5] Li, H., and Ekici, K., "A Novel Approach for Flutter Prediction of Pitch–Plunge Airfoils Using an Efficient One-Shot Method," *Journal of Fluids and Structures*, Vol. 82, 2018, pp. 651–671. doi:10.1016/j.jfluidstructs.2018.08.012, URL https://doi.org/10.1016/j.jfluidstructs.2018.08.012.

[6] He, S., Jonsson, E., Mader, C. A., and Martins, J. R. R. A., "Coupled Newton–Krylov Time-Spectral Solver for Flutter and Limit Cycle Oscillation Prediction," *AIAA Journal*, Vol. 59, No. 6, 2021, pp. 2214–2232. doi:10.2514/1.J059224.

[7] Li, J., He, S., Zhang, M., Martins, J. R. R. A., and Khoo, B. C., "Physics-Based Data-Driven Buffet-Onset Constraint for Aerodynamic Shape Optimization," *AIAA Journal*, Vol. 60, No. 8, 2022, pp. 4775–4788. doi:10.2514/1.J061519.

[8] Timme, S., "Global instability of wing shock-buffet onset," *Journal of Fluid Mechanics*, Vol. 885, 2020, p. A37. doi:10.1017/jfm.2019.1001.

[9] Kuznetsov, Y. A., *Elements of Applied Bifurcation Theory*, Springer New York, 2004. doi:10.1007/978-1-4757-3978-7.

[10] MARQUET, O., SIPP, D., and JACQUIN, L., "Sensitivity analysis and passive control of cylinder flow," *Journal of Fluid Mechanics*, Vol. 615, 2008, pp. 221–252. doi:10.1017/s0022112008003662.

[11] Mettot, C., Renac, F., and Sipp, D., "Computation of Eigenvalue Sensitivity to Base Flow Modifications in a Discrete Framework: Application to Open-Loop Control," *Journal of Computational Physics*, Vol. 269, 2014, pp. 234–258. doi:10.1016/j.jcp.2014.03.022.

[12] Shi, Y., Mader, C. A., He, S., Halila, G. L. O., and Martins, J. R. R. A., "Natural Laminar-Flow Airfoil Optimization Design Using a Discrete Adjoint Approach," *AIAA Journal*, Vol. 58, No. 11, 2020, pp. 4702–4722. doi:10.2514/1.J058944.

[13] Kenway, G. K. W., Kennedy, G. J., and Martins, J. R. R. A., "Scalable Parallel Approach for High-Fidelity Steady-State Aeroelastic Analysis and Adjoint Derivative Computations," *AIAA Journal*, Vol. 52, No. 5, 2014, pp. 935–951. doi:10.2514/1.J052255.

[14] Boullé, N., Farrell, P. E., and Rognes, M. E., "Optimal Control of Hopf Bifurcations," , 2022. doi:10.48550/arXiv.2201.11684, URL https://arxiv.org/abs/2201.11684.

[15] Boullé, N., Farrell, P. E., and Paganini, A., "Control of Bifurcation Structures Using Shape Optimization," *SIAM Journal on Scientific Computing*, Vol. 44, No. 1, 2022, pp. A57–A76. doi:10.1137/21M1418708.

[16] He, S., Shi, Y., Jonsson, E., and Martins, J. R. R. A., "Eigenvalue Problem Derivatives Computation for a Complex Matrix Using the Adjoint Method," *Mechanical Systems and Signal Processing*, Vol. 185, 2023, p. 109717. doi:10.1016/j.ymssp.2022.109717.

[17] Martins, J. R. R. A., Sturdza, P., and Alonso, J. J., "The Complex-Step Derivative Approximation," *ACM Transactions on Mathematical Software*, Vol. 29, No. 3, 2003, pp. 245–262. doi:10.1145/838250.838251.

[18] Slotine, J.-J. E., and Li, W., *Applied Nonlinear Control*, Prentice Hall, Englewood Cliffs, NJ, 1991.

[19] Elman, H. C., Meerbergen, K., Spence, A., and Wu, M., "Lyapunov Inverse Iteration for Identifying Hopf Bifurcations in Models of Incompressible Flow," *SIAM Journal on Scientific Computing*, Vol. 34, No. 3, 2012, pp. A1584–A1606. doi:10.1137/110827600.

[20] Timme, S., Badcock, K. J., Wu, M., and Spence, A., "Lyapunov Inverse Iteration for Stability Analysis Using Computational Fluid Dynamics," *53rd AIAA/ASME/ASCE/AHS/ASC Structures, Structural Dynamics and Materials Conference*, American Institute of Aeronautics and Astronautics, 2012. doi:10.2514/6.2012-1547.

[21] Roose, D., and Hlavaček, V., "A Direct Method for the Computation of Hopf Bifurcation Points," *SIAM Journal on Applied Mathematics*, Vol. 45, No. 6, 1985, pp. 879–894. doi:10.1137/0145053.

[22] Lambe, A. B., and Martins, J. R. R. A., "Extensions to the Design Structure Matrix for the Description of Multidisciplinary Design, Analysis, and Optimization Processes," *Structural and Multidisciplinary Optimization*, Vol. 46, No. 2, 2012, pp. 273–284. doi:10.1007/s00158-012-0763-y.

[23] Zhu, Y., Wang, Y., Zhang, X., and Kang, Z., "A New Form of Forbidden Frequency Band Constraint for Dynamic Topology Optimization," *Structural and Multidisciplinary Optimization*, Vol. 65, No. 4, 2022. doi:10.1007/s00158-022-03220-1.

[24] Linnainmaa, S., "Taylor Expansion of the Accumulated Rounding Error," *BIT*, Vol. 16, No. 2, 1976, pp. 146–160. doi:10.1007/BF01931367.

[25] Martins, J. R. R. A., and Ning, A., *Engineering Design Optimization*, Cambridge University Press, Cambridge, UK, 2022. doi:10.1017/9781108980647, URL `https://mdobook.github.io`.

[26] Lyu, Z., Xu, Z., and Martins, J. R. R. A., "Benchmarking Optimization Algorithms for Wing Aerodynamic Design Optimization," *Proceedings of the 8th International Conference on Computational Fluid Dynamics*, Chengdu, Sichuan, China, 2014. ICCFD8-2014-0203.

[27] Gray, J. S., Hwang, J. T., Martins, J. R. R. A., Moore, K. T., and Naylor, B. A., "OpenMDAO: An open-source framework for multidisciplinary design, analysis, and optimization," *Structural and Multidisciplinary Optimization*, Vol. 59, No. 4, 2019, pp. 1075–1104. doi:10.1007/s00158-019-02211-z.

[28] Yildirim, A., Gray, J. S., Mader, C. A., and Martins, J. R. R. A., "Coupled Aeropropulsive Design Optimization of a Podded Electric Propulsor," *AIAA Aviation Forum*, 2021. doi:10.2514/6.2021-3032.

[29] Gill, P. E., Murray, W., and Saunders, M. A., "SNOPT: An SQP algorithm for large-scale constrained optimization," *SIAM Journal of Optimization*, Vol. 12, No. 4, 2002, pp. 979–1006. doi:10.1137/S1052623499350013.

[30] Wu, N., Kenway, G., Mader, C. A., Jasa, J., and Martins, J. R. R. A., "pyOptSparse: A Python framework for large-scale constrained nonlinear optimization of sparse systems," *Journal of Open Source Software*, Vol. 5, No. 54, 2020, p. 2564. doi:10.21105/joss.02564.

[31] Sahin, M., and Owens, R. G., "A numerical investigation of wall effects up to high blockage ratios on two-dimensional flow past a confined circular cylinder," *Physics of Fluids*, Vol. 16, No. 5, 2004, pp. 1305–1320. doi:10.1063/1.1668285.

[32] Rajani, B. N., Kandasamy, A., and Majumdar, S., "Numerical Simulation of Laminar Flow Past a Circular Cylinder," *Applied Mathematical Modelling*, Vol. 33, No. 3, 2009, pp. 1228–1247. doi:10.1016/j.apm.2008.02.019.

[33] Franke, R., Rodi, W., and Schönung, B., "Numerical Calculation of Laminar Vortex-Shedding Flow Past Cylinders," *Journal of Wind Engineering and Industrial Aerodynamics*, Vol. 35, 1990, pp. 237–257. doi:10.1016/0167-6105(90)90219-3.

[34] Williamson, C. H. K., "Vortex Dynamics in the Cylinder Wake," *Annual Review of Fluid Mechanics*, Vol. 28, No. 1, 1996, pp. 477–539. doi:10.1146/annurev.fl.28.010196.002401.

[35] He, S., Shi, Y., Jonsson, E., and Martins, J. R. R. A., "Eigenvalue problem derivatives computation for a complex matrix using the adjoint method," *Mechanical Systems and Signal Processing*, Vol. 185, 2023, p. 109717. doi:10.1016/j.ymssp.2022.109717.

[36] Barkley, D., "Linear analysis of the cylinder wake mean flow," *Europhysics Letters (EPL)*, Vol. 75, No. 5, 2006, pp. 750–756. doi:10.1209/epl/i2006-10168-7.

[37] SIPP, D., and LEBEDEV, A., "Global stability of base and mean flows: a general approach and its applications to cylinder and open cavity flows," *Journal of Fluid Mechanics*, Vol. 593, 2007, pp. 333–358. doi:10.1017/s0022112007008907.

[38] Jacquin, L., Molton, P., Deck, S., Maury, B., and Soulevant, D., "Experimental Study of Shock Oscillation over a Transonic Supercritical Profile," *AIAA Journal*, Vol. 47, No. 9, 2009, pp. 1985–1994. doi:10.2514/1.30190.

[39] Sartor, F., Mettot, C., and Sipp, D., "Stability, Receptivity, and Sensitivity Analyses of Buffeting Transonic Flow over a Profile," *AIAA Journal*, Vol. 53, No. 7, 2015, pp. 1980–1993. doi:10.2514/1.j053588.

[40] CROUCH, J. D., GARBARUK, A., MAGIDOV, D., and TRAVIN, A., "Origin of transonic buffet on aerofoils," *Journal of Fluid Mechanics*, Vol. 628, 2009, pp. 357–369. doi:10.1017/s0022112009006673.

[41] Crouch, J., Ahrabi, B., and Kamenetskiy, D., "Weakly nonlinear behaviour of transonic buffet on airfoils," *Journal of Fluid Mechanics*, Vol. 999, 2024. doi:10.1017/jfm.2024.499.